Dalton Transactions

ROYAL SOCIETY OF CHEMISTRY

PAPER

View Article Online
View Journal | View Issue

Cite this: *Dalton Trans.*, 2022, **51**, 16486

Modulation of the magnetic and photophysical properties in 3d–4f and 4f–4f′ heterobimetallic complexes involving a tetrathiafulvalene-based ligand†

Haiet Douib,[a,b] Jessica Flores Gonzalez,[a] Saskia Speed,[c,d] Vincent Montigaud,[a] Bertrand Lefeuvre,[a] Vincent Dorcet,[a] François Riobé, [c] Olivier Maury, [c] Abdelkrim Gouasmia,[b] Boris Le Guennic, [a] Olivier Cador *[a] and Fabrice Pointillart *[a]

The reaction between the 2-(1-(2,6-di(pyrazol-1-yl)-4-methylpyridyl)-4,5-(4,5-bis(propylthio)-tetrathiafulvalenyl)-1*H*-benzimidazol-2-yl)-pyridine ligand (L), 1 equivalent of $Ln(hfac)_3{\cdot}2H_2O$/$Dy(tta)_3{\cdot}2H_2O$ ($hfac^-$ = 1,1,1,5,5,5-hexafluoroacetylacetonate, tta^- = 2-thenoyltrifluoroacetonate) and $M(hfac)_2{\cdot}2H_2O$ leads to the formation of heteroleptic 3d–4f dinuclear complexes of formula $[MLn(hfac)_5(L)]_n$ (M(II) = Cd, Zn, Co, Mn, Ni and Ln(III) = Dy, Yb, Nd) and $[ZnDy(tta)_2(hfac)_3(L)]{\cdot}(CH_2Cl_2)$. Their X-ray structures reveal that the two coordination sites are occupied by one Ln(III) ion and one M(II) transition metal respectively. The M(II) ions are coordinated to the benzoimidazolylpyridine (bzip) moiety in a N_2O_4 coordination sphere, while the Ln(III) ions are coordinated to the 2,6-di(pyrazol-1-yl)-4-pyridine (dpp) moiety in a N_3O_6 surrounding. When Dy(III) ion is used a field-induced Single-Molecule Magnet (SMM) behavior is detected with a magnetic relaxation time slightly dependent to the nature of the vicinal divalent transition metal. On the other hand, when the Yb(III) is used, intense, moderated or quenched $^2F_{5/2} \rightarrow {}^2F_{7/2}$ NIR luminescence is observed when the Yb(III) ion is respectively associated with the Zn(II), Mn(II) and Ni(II)/Co(II) ion. The emission intensity can be modulated in function of the metal-to-ligand charge transfer and d–d transition intensities. The replacement of the divalent transition metal by a trivalent lanthanide leads to the formation of heteroleptic 4f–4f′ dinuclear complexes of formula $[Ln_{2-x}Ln'_x(hfac)_6(L)]{\cdot}a(CH_2Cl_2){\cdot}b(C_6H_{14})$ and $[Dy_{1.11}Nd_{0.89}(tta)_3(hfac)_3(L)]$. The coordination selectivity is based on the radius. Among the 4f–4f′ series, the Dy(III) derivatives displayed such ion in N_2O_6 eight-coordinated sphere allowing the observation of SMM behavior. The three compounds $[Dy_{1.21}Nd_{0.79}(hfac)_6(L)]{\cdot}2(CH_2Cl_2){\cdot}(C_6H_{14})$, $[Yb_{1.04}Nd_{0.96}(hfac)_6(L)]$ and $[YbPr(hfac)_6(L)]$ displayed respectively Nd(III), modarated Yb(III) and intense Yb(III) NIR emissions.

Received 21st July 2022,
Accepted 3rd October 2022

DOI: 10.1039/d2dt02375j

rsc.li/dalton

Introduction

The great success of the use of lanthanide ions in coordination chemistry and in the design of supramolecular edifices comes from their intrinsic multiple properties *i.e.* magnetic and optical properties.[1,2] On the one hand, the high magnetic moment and strong magnetic anisotropy were exploited in the molecular magnetism field of research to design Single

[a]*Institut des Sciences Chimiques de Rennes UMR 6226 CNRS-UR1, Université de Rennes 1, 35042 Rennes Cedex, France. E-mail: olivier.cador@univ-rennes1.fr, fabrice.pointillart@univ-rennes1.fr*
[b]*Laboratoire des Matériaux Organiques et Hétérochimie (LMOH), Département des sciences de la matière, Université Larbi Tébessi de Tébessa, Route de Constantine 12002, Tébessa, Algeria*
[c]*ENSL, CNRS, Laboratoire de Chimie UMR 5182, 46 allée d'Italie, 69364 Lyon, France*
[d]*Departament de Química Inorgànica i Orgànica, Secció de Química Inorgànica, Universitat de Barcelona, Martí i Franquès 1-11, 08028 Barcelona, Spain*

†Electronic supplementary information (ESI) available: Experimental details for synthesis and physical characterisation. Crystallographic information in CIF format, Ortep view of **1**, **3**, **4**, **6**, **8**, **11**, **13**, **15**, **17–19** (Fig. S1–S5, S10, S12, S14, S17–S20 and S22), packing views of **3**, **4**, **6**, **8**, **11**, **17–19** (Fig. S6–S9, S11, S13, S15, S16, S21 and S23), cyclic voltammetry for compounds **1–13** (Fig. S24) and **14–19** (Fig. S25), visible absorption in CH_2Cl_2 solution (Fig. S26 and S27), in KBr solid-state (Fig. S28 and S29), visible emission at room temperature and 77 K (Fig. S30–S43), dc magnetic data (Fig. S44–S58) and ac magnetic data (Fig. S59–S79). X-ray crystallographic data (Tables S1–S4 and S6–S8), SHAPE analysis (Tables S5 and S9), oxidation potentials (Table S10) and additional ac parameters (Tables S11–S17). CCDC 1865127–1865130 and 1865135–1865140. For ESI and crystallographic data in CIF or other electronic format see DOI: https://doi.org/10.1039/d2dt02375j

Molecule Magnets (SMMs) and targeted potential applications such as high-density data storage devices, quantum computing or spintronics.[3–8] On the other hand, their specific luminescence ranging from the UV-visible to the Near Infrared (NIR) region, make lanthanide-based coordination complexes suitable for a plethora of other applications in the fields of OLEDs,[9] time-resolved fluoro-immunoassays,[10] biosensors[11,12] and time-resolved imaging.[13,14]

For both research fields, a challenge is to find efficient strategies to enhance the performance of these aforementioned properties. In a magnetic point of view, chemists combined 3d and 4f ions in order to combine the advantages of the two ions *i.e.* strong magnetic anisotropy of the 4f elements with significant magnetic interactions with the paramagnetic 3d elements[15–18] and even quenching of the Quantum Tunneling of Magnetization (QTM).[19] It is worth to notice that even the association with diamagnetic transition metals could lead to enhancement of the magnetic properties due to its electrostatic effect on the magnetic anisotropy of the 4f elements.[20–22] Such electrostatic effect can be induced by trivalent lanthanide ions as demonstrated by M.-L. Tong in 2013.[23–25] In other special cases, the 3d site can highlight exciting magnetic properties such as spin-crossover and influence the whole physical properties of the system.[26] In an photophysic point of view, the emitting f excited states have very weak absorption coefficients with long lifetimes due to the Laporte rules.[27] Thus direct sensitization is not efficient for 4f luminescence especially in diluted solution, and strategies based on the use of organic chromophores, which strongly absorb light in the UV-visible range, have been developed:[28] (i) triplet excited-state sensitization, (ii) singlet excited-state with intra-ligand charge transfer (ILCT) which has been intensively used in the case of push–pull ligands such as tetrathiafulvalene (TTF) functionalized derivatives[29] (iii) intramolecular f → f energy transfer process[30,31] and (iv) induced triplet metal-to-ligand charge transfer (MLCT). As previously listed, one of the strategies to sensitize the luminescence is to inject transition metals in the architecture, for example a diamagnetic Zn(II)-Schiff base unit was used as an organometallic antenna for visible luminescence sensitization,[32] while diamagnetic Pt(II) and Ru(II), and even paramagnetic Cr(III) were used to extend the lifetimes of NIR luminescence[33] and optimization of molecular light-upconversion.[34] On the contrary, paramagnetic transition metals are described as potential quenchers the 4f luminescence.[35]

Consequently, it is easy to be convinced that d–4f and 4f–4f′ heterobimetallic complexes could be a promising strategy to enhance both magnetic and optical properties but the challenge is to succeed to selectively coordinate the two different metal ions. To reach a perfect control of the step-by-step synthesis of the final targets, the chemists elaborated metalloligand approach[36–38] and multi-coordination-site ligands. For the second strategy, chemists played with the size, charge, denticity, and hard/soft hetero-atoms of the coordinating units. The most famous examples of such ligands are the pseudo-helicenic ligands based on the tridentate chelating 6-(carbamoyl)pyridine-2-yl-1*H*-benzimidazole and bidentate chelating

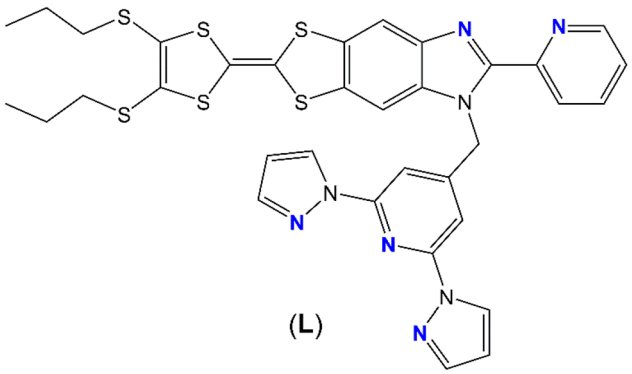

Scheme 1 Molecular structure of ligand **L** highligting the two sites of coordination.

pyridine-2-yl-1alkylbenzimidazole moieties developed by the group of C. Piguet,[26,39–41] the Schiff Base ligands such as Salicylideneimine derivatives[42–47] and the macrocycle derived from 1,4,7,10-tetraazadodecane-1,4,7,10-tetraacetic acid (DOTA) derivated ligands.[48] Using the latter family of ligands decorated with a TTF core, some of us succeeded to elaborate 3d–4f heterobimetallic complexes.[49,50] Then we developed the synthesis of a TTF-based ligand involving one bis-chelating (bzip = benzimidazol-2-yl-pyridyl) and one tris-chelating (dpp = di-(pyrazol-1-yl)-4-pyridyl) coordination site for the design of homoleptic Dy(III) and Yb(III) complexes which displayed multi-SMM behavior[51] and multi-emission[52] in a single molecule.

In this article, we go one step forward using the previously mentioned 2-{1-[2,6-di(pyrazol-1-yl)-4-methylpyridyl]-4,5-[4,5-bis(propylthio)-tetrathiafulvalenyl]-1*H*-benzimidazol-2-yl}pyridine ligand (**L**) (Scheme 1) to design heteroleptic *n*d-4f (*n* = 3, 4) and 4f–4f′ complexes. These complexes have been characterized by X-ray diffraction, absorption spectroscopy and cyclic voltammetry.

The magnetic and emission properties of the complexes as well as the influence of the two associated metal ions were investigated.

Results and discussion

Synthesis

The **L** ligand was selected to design heterobimetallic complexes due to its two sites of coordination with different denticities.

The first part of this article is focused on the design of 3d–4f heterobimetallic complexes. To do so, the first step consisted in the coordination of the d transition metal ($M(hfac)_2{\cdot}2H_2O$) which must be coordinated to the bidentate chelating site (benzimidazole-2-yl-pyridine, bzip) of **L**. The second step consisted in the coordination of the 4f element ($Ln(hfac)_3{\cdot}2H_2O$) to the remaining free tridentate chelating site of coordination (2,6-di(pyrazol-1-yl)-4-methylpyridine, dpp). The combination of the coordination number limitation of the d element and the non-lability of such element guarantees a optimal selectivity of the coordination for d and f elements on

the bzip and dpp moieties, respectively. Finally, the $Dy(hfac)_3{\cdot}2H_2O$ was replaced by the $Dy(tta)_3{\cdot}2H_2O$ precursor keeping the same step-by-step protocol in order to evaluate the lability of the ancillary ligands in case of 3d ions. The step-by-step synthetic strategy was selected to be on line with the one used for the f–f′ complexes.

The second part of the article is focused on the design of 4f–4f′ heterobimetallic complexes. To reach this more challenging aim, the preference of the large lanthanide for the dpp site of coordination was demonstrated with the selective coordination of the Pr(III) ion in **14**. The coordination selectivity is demonstrated at room temperature while heating the reaction mixture led to the coordination of the two bzip and dpp sites (see ESI† for X-ray structure of $[Nd_2(hfac)_6(L)]{\cdot}C_6H_{14}$ (**18**)). After the selective coordination of the larger lanthanide (Nd(III)) on the dpp site, the smaller lanthanide (Dy(III)) was added for coordination to the bpiz site. The ratio between the two lanthanide ions are determined by Energy Dispersive Spectrometry (EDS) and given values are the average value between at least three measurements (see ESI† for details). This first step by step strategy lead to the formation of the $[Dy_{1.21}Nd_{0.79}(hfac)_6(L)]{\cdot}2(CH_2Cl_2){\cdot}(C_6H_{14})$ (**15**) compound. In order to increase the discrimination between the two sites, three strategies were used: (i) playing with the size of the ancillary ligand *i.e.* the $Dy(hfac)_3{\cdot}2H_2O$ was replaced by $Dy(tta)_3{\cdot}2H_2O$, (ii) using a smaller lanthanide than Dy(III), *i.e.* the $Dy(hfac)_3{\cdot}2H_2O$, was replaced by $Yb(hfac)_3{\cdot}2H_2O$ and (iii) using simultaneously a smaller lanthanide than Dy(III) (*i.e.* Yb(III)) and a bigger lanthanide than Nd(III) (*i.e.* Pr(III)). From isolated single crystals, one could notice that the first strategy led to the formation of the $[Dy_{1.11}Nd_{0.89}(tta)_3(hfac)_3(L)]$ (**16**) compound while the second strategy led to the $[Yb_{1.04}Nd_{0.96}(hfac)_6(L)]$ (**17**) compound, and finally the third strategy lead to $[YbPr(hfac)_6(L)]$ (**19**). It is worth to notice that the latter compound can also be obtained starting from complex **14**. The three strategies have been a success increasing the discrimination.

Crystal structure analysis

The whole series of compounds **1–10** possesses a similar molecular structure, the differences come from the crystallization space group which depends on the number and the nature of the interstitial solvent molecules. The latter ones depend of the size of the 3d and 4f metal ions. Consequently a general description of the structure is given for the whole series and only the significant structural changes are point out.

$[MLn(hfac)_5(L)]_n{\cdot}x(CH_2Cl_2){\cdot}y(C_6H_{14}){\cdot}z(H_2O)$. The X-ray crystallographic data for compounds **1–10** are given in Tables S1 and S3.† The Ortep views for the compounds **1–10** are depicted in Fig. S1–S5.† All X-ray structures are composed of one $M(hfac)_2$ and one $Ln(hfac)_3$ moieties coordinated to the ligand L. The $M(hfac)_2$ is selectively coordinated to the bidentate chelating benzimidazole-2-yl-pyridine (bzip) coordination site while the $Ln(hfac)_3$ is coordinated to the tridentate chelating 2,6-di(pyrazol-1-yl)-4-methylpyridine (dpp) coordination site (Fig. 1). The Ln1 ion is surrounded by six oxygen atoms that belong to three $hfac^-$ ligands and three nitrogen atoms from the dpp coordination site of **L**.

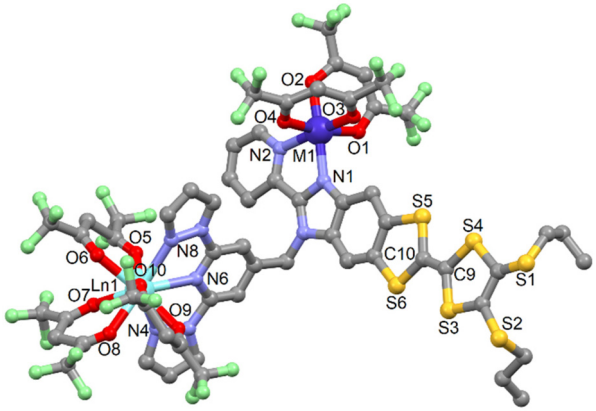

Fig. 1 Representative molecular structure of the series of compounds **1–10** (M = Cd, Zn, Mn, Co and Ni; Ln = Dy and Yb). Hydrogen atoms and solvent molecules of crystallization are omitted for clarity.

The M1 ion is surrounded by four oxygen atoms that belong to two $hfac^-$ ligands and two nitrogen atoms from the bzip coordination site of **L**. The average Ln–O distances are shorter than the average Ln–N distances (Table S4†) due to the oxophilic character of the lanthanide, as usually observed. At the transition metal level, the difference of bond lengths between M–O and M–N are not as significant as for the lanthanide ions (Table S4†). The arrangement of the ligands around the lanthanide ions leads to a spherical tricapped trigonal prism (D_{3h} symmetry) and spherical capped square antiprism (D_{2d} symmetry) as coordination polyhedra (Table S5†). The distortion is visualized by continuous shape measures performed with SHAPE 2.1 (Table S5†).[53] The central C=C bond lengths of the TTF core confirm the neutral form of **L** in all the compounds **1–10**.

The crystal packing reveals the formation of head-to-tail dimers of **L** (called Donor–Acceptor dimers, D–A). Then each D–A dimer forms a column of **L** along the *a* axis thanks to Donor–Donor (D–D) interaction through S···S short contacts (Fig. 2 and S6–S9, Table S6†). Finally each column is separated by the $Ln(hfac)_3$ and $M(hfac)_2$ units along the *b* and *c* axis, respectively. The shortest intermolecular Ln–Ln distances as well as the M–Ln inter- and intra-molecular distances are listed in Table S6.† It is worth to notice that the most important structural differences in this series are observed in the case of **1**. In fact one of the ligands is clearly more distorted with an α value lower than for the other 3d4f hetero-bimetallic compounds and a stronger overlap between the head-to-tail π systems of **L** allowing the formation of short S11···O2 contacts (Table S6†).

$[ZnDy(tta)_2(hfac)_3(L)]{\cdot}(CH_2Cl_2)$ (11). **11** crystallizes in the $P\bar{1}$ (no. 2) triclinic space group (Table S1†). The asymmetric unit is composed by one molecule of $[ZnDy(tta)_2(hfac)_3(L)]$ and one crystallization molecule of dichloromethane. An Ortep view of **11** is depiced in Fig. S10.† The X-ray structures revealed that the Zn(II) and Dy(III) ions are respectively coordinated to the

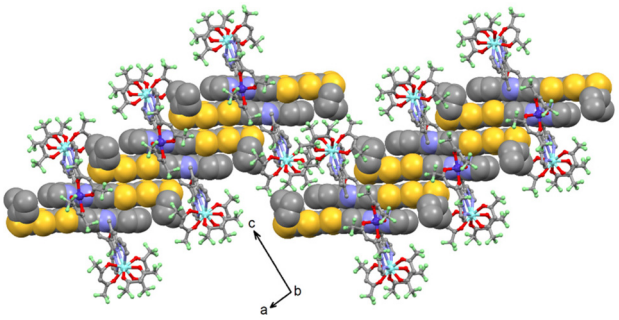

Fig. 2 Representative crystal packing of the series of compounds **1–10**. The {4,5-[4,5-bis(propylthio)-tetrathiafulvalenyl]-1*H*-benzimidazol-2-yl} pyridine fragment is shown in spacefill representation while the dpp moiety and the organometallic precursors $M(hfac)_2$ and $Ln(hfac)_3$ are shown in ball and sticks representation.

bzip and dpp fragments as expected. Nevertheless the starting nature of the precursors *i.e.* $Zn(hfac)_2$ and $Dy(tta)_3$ do not remain intact. In fact a reorganisation of the β-diketonate anions is observed so that the steric hindrance around the metal is optimal.

Consequently, the comproportionation reaction leads to the formation of Zn(hfac)(tta) and $Dy(hfac)_2(tta)$ units that are coordinated to the bzip and dpp sites (Fig. 3). Such reorganisation was already observed for the design of homo-metallic lanthanide complexes involving **L** starting from the $Dy(hfac)_3$ and $Dy(tta)_3$ precursors.[51]

The Zn(II) and Ln(III) ions remain in N_2O_4 and N_3O_6 environment. The arrangement of the ligands around the lanthanide ion leads to a spherical tricapped trigonal prism (D_{3h} symmetry) as coordination polyhedra (Table S5†).[53] The reorganization of the ancillary ligands does not induce significant changes in the M–X and Ln–X (X = O and N) distances (Table S4†) neither in the crystal packing in which the formation of columns involving D–D and D–A dimers is observed (Table S6 and Fig. S11†).

$[Pr(hfac)_3(L)]_2{\cdot}0.5(C_6H_{14}){\cdot}0.25(CH_2Cl_2)$ (14). Compound **14** crystallizes in the *C*2/*c* (no. 15) monoclinic space group (Table S1†). The asymmetric unit is composed by two $[Pr(hfac)_3(\mathbf{L})]$ molecules and half a crystallization molecule of hexane (Fig. 4).

The X-ray structure reveals that only the tris-chelating coordination site (dpp moiety) of **L** is coordinated to one $Pr(hfac)_3$ moiety. This selectivity can be explained by the larger ionic radius of the Pr(III) ion which is too large to fit in the bis-coordinating site. Complex **14** nicely illustrates the preference of lanthanide ions to one specific coordination sites. The Pr(III) ion is surrounded by six oxygen atoms that belong to three $hfac^-$ ligands and three nitrogen atoms coming from the tris-chelating coordination site (dpp moiety). The average Pr–O distances are shorter (2.479(10) Å) than the average Pr–N distances (2.649(11) Å) (Table S7†). The arrangement of the ligands leads to distorted spherical tricapped trigonal prism (D_{3h}) and Muffin (Cs) as coordination polyhedra for the Pr1 and Pr2 ions, respectively (Table S5†). The central C=C bonds of the TTF cores are equal to 1.324(2) Å which confirms the neutral form of **L**. The two crystallographically independent complexes form dimers by short S···S contacts (S4···S9 = 3.714 Å, S4···S10 = 3.719 Å, S5···S11 = 3.714 Å and S5···S12 = 3.732 Å) (Table S8†). The crystal packing reveals that the dimers further arrange as dimers of dimers isolated by $Pr(hfac)_3$ units, with the shortest S···S contacts being S6···S7 = 3.645 Å and S6···S10 = 3.696 Å (Fig. S16†). The shortest intermolecular Pr–Pr distance is 9.592 Å (Pr1–Pr2). Compound **14** can be seen as an intermediate to obtain heterobimetallic complexes in which the Pr^{III} ion or lightest lanthanide could be associated with another 4f metal ion.

$[Ln_{1+x}Nd_{1-x}(hfac)_6(L)]{\cdot}2CH_2Cl_2{\cdot}C_6H_{14}$ (Ln = Dy, x = 0.21 (15); Ln = Yb, x = 0.04 (17); Ln = Nd, x = 0 (18)) and $[YbPr(hfac)_6(L)]$ (19). These four compounds are isostructural to the two homometallic complexes of Yb(III) and Dy(III) ions that some of us previously published (Fig. 5).[51,52] All compounds crystallize in the $P2_1/n$ (no. 14) monoclinic space group (Table S2†). The asymmetric unit is composed of two $Ln(hfac)_3$ moieties, one **L** ligand, a *n*-hexane and two dichloromethane molecules of crys-

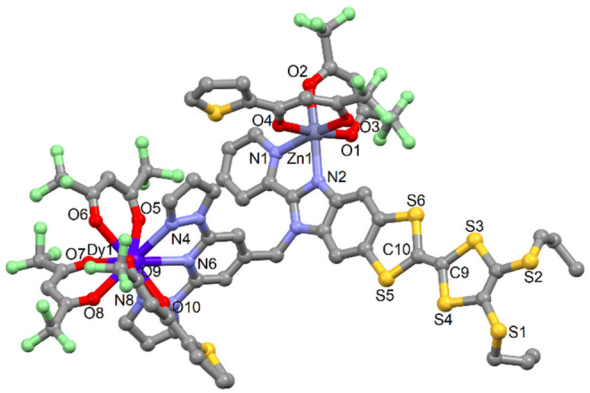

Fig. 3 Molecular structure of **11**. Hydrogen atoms and solvent molecules of crystallization are omitted for clarity.

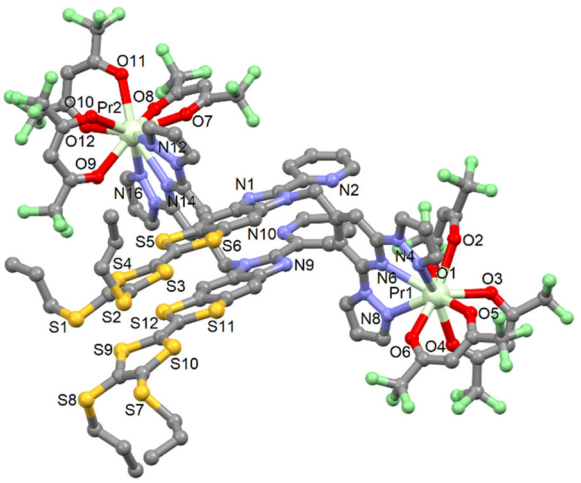

Fig. 4 Molecular structure of **14**. Hydrogen atoms and solvent molecules of crystallization are omitted for clarity.

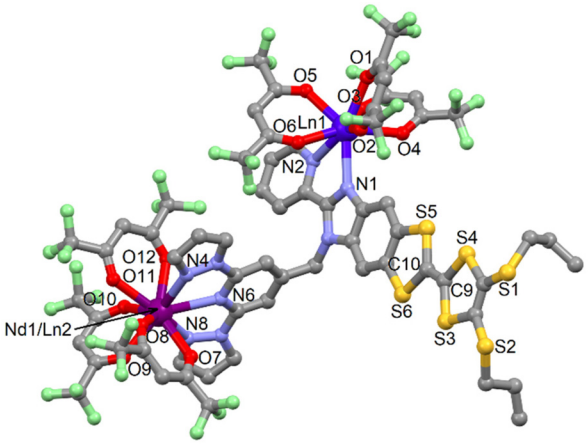

Fig. 5 Representative molecular structure of compounds **15** and **17–19**. Hydrogen atoms and solvent molecules of crystallization are omitted for clarity.

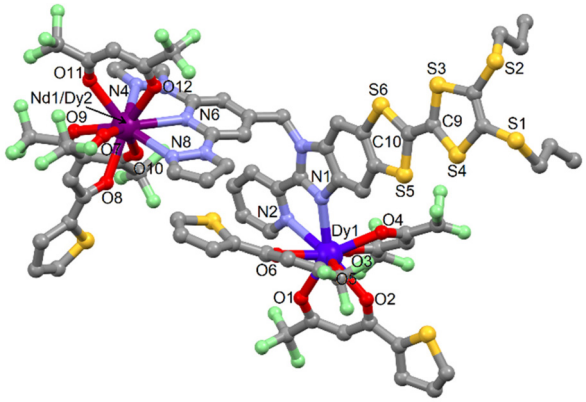

Fig. 6 Molecular structure of **16**. Hydrogen atoms are omitted for clarity.

tallization (Fig. S17–S20† for **15**, **17**, **18** and **19**, respectively). The two lanthanide ions are coordinated to the bzip and dpp moieties in N_2O_6 and N_3O_6 coordination sphere, respectively. Thus the two coordination sites are occupied by a $Ln(hfac)_3$ unit.

The average Ln1–O and Ln1–N distances observed in the eight-coordinated sites respectively in **15** and **17**/**19** are in agreement with those observed in the isostructural $[Dy_2(hfac)_6(\mathbf{L})]\cdot 2CH_2Cl_2\cdot C_6H_{14}$ [51] and $[Yb_2(hfac)_6(\mathbf{L})]\cdot 2CH_2Cl_2\cdot C_6H_{14}$ [52] structures. It thus seems reasonable to consider these sites to be fully occupy by either the Dy(III) and Yb(III) ions. The fraction of Dy or Yb ions in the nine-coordinated site is determined by Scanning Electron Microscopy equal to 21% in **15**, 4% in **17** and close to 0% in **19**. This result shows that the higher the difference of ionic radius between the eight-coordinated lanthanide ion (Ln1) and the nine-coordinated lanthanide ion (Nd1/Ln2), the higher is the selectivity. The arrangement of the ligands leads to a distorted square anti-prism (D_{4d} symmetry) and spherical tricapped trigonal prism (D_{3h} symmetry) as coordination polyhedra for Ln1 and Nd1/Ln2 ions, respectively. The central C=C bond of the TTF core confirms the neutral form of **L**.

The crystal packing reveals the formation of head-to-tail dimers of **L** along the *b* axis (Fig. S21†). A one-dimensional organic network of **L** is formed along this axis thanks to S···S contacts between the head-to-tail dimers (Table S8†). Each column of **L** is separated by the $Ln(hfac)_3$ moieties localized in the nine-coordination sites. The shortest intra- and intermolecular Ln–Ln distances are depicted in Table S7.†

$[Dy_{1.11}Nd_{0.89}(hfac)_3(tta)_3(\mathbf{L})]$ (16). Compound **16** is isostructural to the homo-metallic complex $[Dy_2(hfac)_3(tta)_3(\mathbf{L})]$ which has been previously published by us.[51] The two bis- and tridentate chelating coordination sites of the ligand **L** are occupied by a $[Dy(tta)_2(hfac)]$ and a $[Dy_{0.11}Nd_{0.89}(tta)(hfac)_2]$ unit, respectively (Fig. 6 and S22†). Thus an exchange of one $hfac^-$ and one tta^- anion is observed in complex **16** as for $[Dy_2(hfac)_3(tta)_3(\mathbf{L})]$, demonstrating that such reorganization is not depending on the nature of the lanthanide ion. The eight coordinated lanthanide ion has a D_{4d} N_2O_6 environment while the nine coordinated lanthanide ion has a D_{3h} N_3O_6 environment (Table S9†). More interesting is when the occupancies of the tris-chelating coordination site by each ion is compared to those in **15**. The use of pure $hfac^-$ ancillary ligand leads to an occupancy of 21% of the Dy(III) while the use of a mixture $hfac^-/tta^-$ leads to an occupancy of 11%.

One could notice that even if ligand-scrambling took place, the two remaining coordinated tta-anions to Dy(III) centre led to an increase of the coordination selectivity. In other words, the use of tta^- increases the discrimination between the coordination sites because it favors a perfect match between the size of the two lanthanide ions and the coordination sites for a minimum of steric hindrance. The crystal packing reveals the formation of isolated "head-to-tail" dimers (Fig. S23†).

Electrochemical properties

The redox properties of the complexes **1–19** are investigated by cyclic voltammetry (Fig. S24 and S25†), the values of the oxidation potentials are listed in Table S10.† The cyclic voltammograms for all the complexes show two mono-electronic oxidations at about 0.47–0.67 V for the first oxidation and about 0.90–0.99 V for the second oxidation, corresponding to the formation of a radical cation and a dication TTF fragment, respectively. The electrochemical properties attest that the reversibility of the oxidation potentials and the redox-activity of ligand (**L**) is conserved after complexation.

Photophysical properties

Absorption spectroscopy. The UV-visible absorption properties of the 3d4f heterobimetallic and 4f4f′ heterobimetallic compound series have been studied both in CH_2Cl_2 solution (Fig. S26 and S27†) and KBr solid-state (Fig. S28 and S29†). The UV-visible absorption properties of **L** and the homoleptic Yb(III) derivative (formula $[Yb_2(hfac)_6(\mathbf{L})]\cdot 2CH_2Cl_2\cdot C_6H_{14}$) were previously studied and the attributions of the experimental absorption bands were rationalized by TD-DFT calculations.[49]

Based on those studies, the absorption properties of the two present series of compounds can be described and analysed. The lowest-energy absorption bands in the 17 500–27 500 cm^{-1} energy range were attributed to Intra-Ligand Charge Transfer (ILCT) from the TTF to benzoimidazolpyridine fragment. This ILCT excitation is mainly due to the HOMO to LUMO transition and it is localized at lower energy after complexation of the electron-withdrawing metallic precursors as observed in the solid-state absorption spectra (Fig. S28 and S29†). The red-shift of the ILCT band after complexation attests the integrity of the complexes in CH_2Cl_2 solution. The following energy range of 27 500–35 000 cm^{-1} is constituted of intra-TTF and ILCT excitations as well as Intra-hfac$^-$ transitions (around 33 000 cm^{-1}). It is worth to notice that in this energy range, compound **16** is slightly different than all the other compounds because of the existence of lower-energy Intra-tta$^-$ transitions (around 29 500 cm^{-1}). Finally the highest-energy part of the absorption spectra (above 35 000 cm^{-1}) is devoted to the π–π* intra-dpp transitions.

Emission spectroscopy

3d–4f heterobimetallic complexes (4f = Yb(III)). The emission properties of complexes **3**, **5**, **8** and **10** were studied at room temperature and at 77 K in solid-state. The four samples were irradiated at 350 nm and display a very weak visible fluorescence at room temperature (Fig. S30–S33†). The same irradiation at low temperature (77 K) leads to the phosphorescence of **L** (Fig. S34–S37†). These kind of ligand-centered emission was already observed for ligands involving the {[4,5-bis(propylthio)-tetrathiafulvalenyl]-1*H*-benzimidazol-2-yl}pyridine molecular skeleton.[52,54] More interesting is the emission in the NIR region, complex **3** highlights a characteristic luminescence of the Yb(III) ion, assigned to the $^2F_{5/2} \rightarrow {}^2F_{7/2}$ transition (Fig. 7a). The maximum number of expected contribution for a Yb(III) ion is four taking into account the degeneracy of the $^2F_{7/2}$ Kramer's doublet ground state. These four main bands can be identified centered at 9756, 9852, 10 091, and 10 172 cm^{-1}, but there are also shoulders corresponding either to the presence of two crystallographically independent Yb(III) centers with distinct coordination polyhedron symmetry (Table S5†) leading to two different crystal field splittings and/or additional transitions coming from M_J excited states of the $^2F_{5/2}$ multiplet as frequently observed in previous studies.[52,55,56]

The same light irradiation to complex **5** leads to a similar NIR Yb(III) centered luminescence. The resolution is lower but the four main transition are still observed centered at 9699 cm^{-1}, 9766 cm^{-1}, 9921 cm^{-1}, and 10 183 cm^{-1} (Fig. 7b).

The main difference between **3** and **5** is the stronger intensity of the emission for **3** than for **5**. Finally the NIR luminescence for **8** and **10** is totally quenched. Among the series of 3d4f heterobimetallic compounds, three different optical behaviors can be identified: (1) an intense NIR emission when the Yb(III) ion is associated with the d^{10} closed shell electronic structure Zn(II), (2) a complete quenching of the Yb(III) NIR luminescence the presence Co(II) and Ni(II) ions and (3) a partial quenching in the presence of Mn(II).

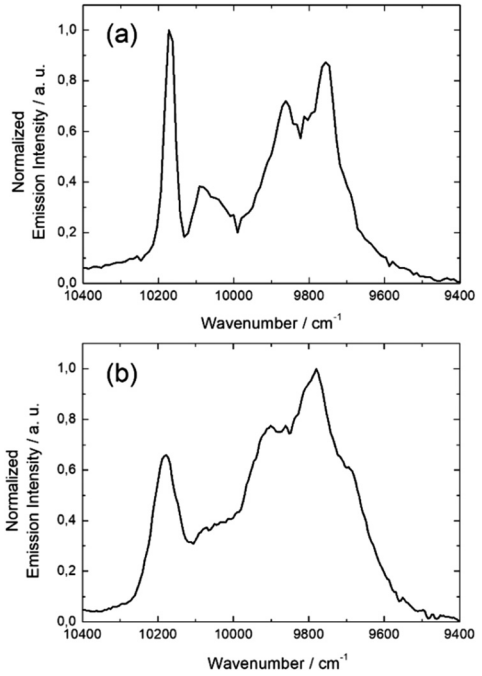

Fig. 7 Solid state NIR luminescence spectrum of **3** (a) and **5** (b) at 77 K, λ_{ex} = 600 nm (16 667 cm^{-1}).

The non-detrimental effect of close shell metal ion like Zn(II) is well established, it mainly acts as Lewis acid red-shifting ILCT transition and contributes to rigidify of the structure restricting nonradiative deactivation processes.[57–59] In marked contrast, paramagnetic transition metals like Cu(II), Co(II), Ni(II) are generally good fluorescence quenchers due to the presence of low-lying d–d and/or Metal–Ligand Charge Transfer (LMCT) state favouring non radiative processes. These metal ions enhance the non radiative desexcitation pathways of the antenna and this later is no more able to sensitise the lanthanide ion resulting in a very strong emission quenching.[60,61] Finally the partial emission quenching observed in the presence of paramagnetic Mn(II) may be due to a moderate spin–orbit coupling, it does not highlight strong MLCT and the weak d–d transitions are higher in energy than the π–π* singlet state. Thus it is does not favor nonradiative decays and compound **5** is one of the rare examples of NIR emitters containing a paramagnetic transition metal.

4f–4f' heterobimetallic complexes. Irradiation at 350 nm at room temperature gives a very weak visible fluorescence for all the compounds (Fig. S38–S40†) while the same irradiation at low temperature (77 K) leads to the phosphorescence of **L** (Fig. S41–S43†). Low-energy irradiation (600 (nm)) at 77 K of **15**, leads to the NIR emission of the Nd(III) ion which is attributed to the classic three excitations localized at 7479 cm^{-1} ($^4F_{3/2} \rightarrow {}^4I_{13/2}$), 9398 cm^{-1} ($^4F_{3/2} \rightarrow {}^4I_{11/2}$) and 11 099 cm^{-1} ($^4F_{3/2} \rightarrow {}^4I_{9/2}$) (Fig. 8a) while no emission of the Dy(III) ion is detected because of the non-energy matching between the emissive level of the Dy(III) ion and the ILCT. Compound **17** is composed of two potentially emissive lanthanides with the

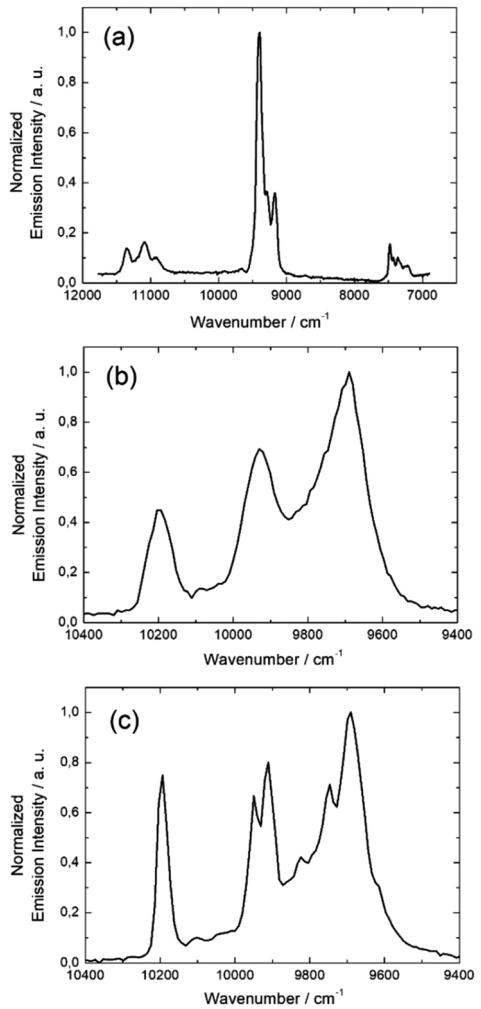

Fig. 8 Solid state NIR luminescence spectra of **15** (a), -**17** (b) and **19** (c) at 77 K, λ_{ex} = 600 nm (16 667 cm^{-1}).

eight coordinated Yb(III) and the nine coordinated Nd(III). Irradiation of **17** at 600 nm at 77 K, leads to a single NIR emission at 9690 cm^{-1}, 9930 cm^{-1} and 10 193 cm^{-1} which is characteristic of the $^2F_{5/2} \rightarrow {}^2F_{7/2}$ transition of the Yb(III) ion (Fig. 8b). Based on the previous works[62–66] and on the much more resolved Yb(III)-centered luminescence (Fig. 8c) once Nd(III) has been changed by a Pr(III) ion in **19**, the absence of Nd(III)-centered emission in **17** might be an indication of an efficient Nd-to-Yb Energy Transfer (ET).

Magnetic properties

Static magnetic measurements. The static magnetic properties of compound **1** are represented on Fig. S44† with the $\chi_M T$ *vs.* T plot and the M *vs.* H plot at 2 K. At room temperature $\chi_M T$ is equal to 13.7 cm^3 K mol^{-1}. This value is slightly smaller than expected for Dy(III) ($^6H_{15/2}$, 14.14 cm^3 K mol^{-1}).[67] On cooling, $\chi_M T$ decreases monotonically according to the thermal population of crystal field levels to end up at 12.3 cm^3 K mol^{-1}; a value relatively close to what is expected for the stabilization of the Ising Kramers doublet $|M_J = \pm 15/2>$ (12.5 cm^3 K mol^{-1}). The assumption of the Ising Kramers doublet ground state is supported by the M *vs.* H curve which saturates at 5$N\beta$ (Fig. S44†). The room temperature values of $\chi_M T$ for compounds **2**, **6**, **7** and **9** are equal to 13.78, 2.73, 17.74 and 14.5 cm^3 K mol^{-1} respectively (Fig. S45†). These values are in good agreement with the expected Curie constants: (1) the diamagnetic Cd(II) ion does not contribute so the Curie constant for **2** is 14.17 cm^3 K mol^{-1}. (2) Y(III) is also diamagnetic so the Curie constant for **6** corresponds to the value expected for octahedral Co(II) (~3 cm^3 K mol^{-1}).[68] (3) The sum of 14.17 cm^3 K mol^{-1} from Dy(III) and ~3 cm^3 K mol^{-1} for Co(II) for **7**. (4) Finally, the sum of 14.17 cm^3 K mol^{-1} from Dy(III) and 1 cm^3 K mol^{-1} for the S = 1 spin of Ni(II). $\chi_M T$'s decrease on cooling for the four compounds according the thermal population of crystal field levels of Dy(III) ion for **2** and single-ion anisotropy of 3d element for **7** and **9**, only the single-ion anisotropy of Co(II) is involved for 6 but with the same consequence. The low temperature limits of $\chi_M T$ are equal 11.53, 1.65, 14.26 and 11.54 cm^3 K mol^{-1} for **2**, **6**, **7** and **9** respectively. The magnetization curves at 2 K are plotted on Fig. S46.† The magnetization saturates for **2** at 5.2$N\beta$. The magnetization linearly increase for **7** and **9** at high field with no saturation. The magnetization curve of **7** matches as expected with the sum of **6** and **2**. The room temperature value of $\chi_M T$ for **3** is equal to 2.16 cm^3 K mol^{-1}. This value is slightly smaller than expected for the multiplet ground state $^2F_{7/2}$ of Yb(III) (2.57 cm^3 K mol^{-1})[67] with a diamagnetic Zn(II) and decreases on cooling down (Fig. S47†) according to the thermal population of the crystal field levels of the lanthanide. The room temperature values of $\chi_M T$ for **4** and **5** are respectively equal to 18.73 and 7.28 cm^3 K mol^{-1} (Fig. S48†). The value for **4** is in good agreement with the presence of an isolated Dy(III) ion and an isolated S = 5/2 isolated spin of Mn(II) ion with g_{Mn} = 2 (expected 14.17 + 4.375 = 18.55 cm^3 K mol^{-1}) while the value for **5** is slightly higher than expected (2.57 + 4.375 = 6.94 cm^3 K mol^{-1}). In a commonplace, $\chi_M T$'s decrease on cooling but one may suppose that it is entirely due to the crystal field effects at the lanthanide site since the spin only 3d^5 Mn(II) is almost unaffected by crystal field and follows the Curie in the whole temperature range. At 2 K, the magnetization saturates at 10.2 and 7.4$N\beta$ for **4** and **5** respectively. For **4** it corresponds to the sum of saturation expected for the Ising ground state of Dy(III) (5$N\beta$) and the saturation for S = 5/2 of Mn(II) (5$N\beta$) (Fig. S49†). For **5**, considering saturation for Mn(II) a saturation for Yb(III) at 2.4$N\beta$ is envisaged which is not too far from the value observed for **6** in which the environment around Yb(III) is similar (N_3O_6). The room temperature values of $\chi_M T$ for **8** (5.56 cm^3 K mol^{-1}) and **10** (3.47 cm^3 K mol^{-1}) are in good agreement with the Curie constants evaluated for Yb(III), Co(II) and Ni(II) (2.57, ~3 and 1 cm^3 K mol^{-1} respectively). While the of $\chi_M T$ on cooling for **8** is the combination of crystal field effects at lanthanide site and the combination of spin–orbit coupling and crystal field effects at *meta* site for **8**, the main decrease is entirely due to Yb(III) with a steep descent at low temperature due to zero-field splitting at Ni(II) site (Fig. S50†).[68] Magnetization for **8** at 2 K and 50 kOe is equal to

4.1$N\beta$ that fits with saturation of **6** (2.12$N\beta$) plus the value observed with the same sample environment in **3** (1.53$N\beta$) (Fig. S51†). Compound **11** can be compared to **1** since in both complexes 3d metal is diamagnetic and the coordination polyhedron around Dy(III) is N_3O_6 with nearly similar CShM values (Table S5†). However, in **11**, part of the $hfac^-$ anions has been substituted by tta^-. It changes the crystal field and so the $\chi_M T$ *vs.* *T* curves do not superimpose. For **11**, $\chi_M T$ starts at 14.1 cm^3 K mol^{-1} at room temperature and finishes at 11.7 cm^3 K mol^{-1} at 2 K and the magnetization does not fully saturate since there is a slight linear increase at high field with 5.2$N\beta$ at 50 kOe and at 2 K (Fig. S52†). The room temperature value of $\chi_M T$ for **14** is equal to 1.4 cm^3 K mol^{-1} which is slightly lower than expected for the $^3H_4$ multiplet ground state of Pr(III) (Fig. S53†). $\chi_M T$ decreases continuously on cooling to reach 0.06 cm^3 K mol^{-1} at 2 K while the magnetization increases linearly with the field at 2 K (Fig. S54†). Interestingly, the χ_M *vs.* *T* curve shows a shoulder around 30 K (Fig. S55†) which attests that the ground state is non magnetic. In first approximation, and despite the two crystallographically independent Pr(III) sites, coordination polyhedra of D_{3h} symmetry can be adopted (Table S5†). In such symmetry, the zero field spin Hamiltonian has to be considered with $\widehat{O_k^q}$ the Stevens operators which can expressed as polynomials of the total angular momentum matrices (J^2, J_z, J_+ and J_-).[68,69]

$$\hat{H} = B_2^0\widehat{O_2^0} + B_4^0\widehat{O_4^0} + B_6^0\widehat{O_6^0} + B_6^6\widehat{O_6^6}$$

The parameters to adjust are B_k^q's. The best fit is obtained with B_2^0 = 5.5 cm^{-1}, $B_4^0 = 2.4 \times 10^{-3}$ cm^{-1}, $B_6^0 = 6.1 \times 10^{-5}$ cm^{-1} and B_6^6 = 0.1 cm^{-1}, and a small amount of paramagnetic impurities (χ_{imp} = 0.022 cm^3 mol^{-1}) to account for the monotonic increase of χ_M *vs.* *T* curve at lowest temperatures (Fig. S54†). Analysis reveal that the ground state singlet is non magnetic and is a mixture of the two $M_J = \pm 3$ components of the ground state multiplet $^3H_4$ of Pr(III) as a result of the strong transverse component $\widehat{O_6^6}$ which mixes states with $|\Delta M_J| = 6$. Field variation of the magnetization for **14** at 2 K is quasi linear and well reproduced by the simulated curve obtained with previously fitted parameters (Fig. S54†). $\chi_M T$ *vs.* *T* plot for compound **15** is represented on Fig. S55.† At room temperature $\chi_M T$ is equal to 20.44 cm^3 K mol^{-1} which is much higher than the Curie limit expected for one Dy(III) ion in the octa-coordinated site ($^6H_{15/2}$: 14.17 cm^3 K mol^{-1}) plus one Nd(III) ion in the nona-coordinated site ($^4I_{9/2}$: 1.64 cm^3 K mol^{-1}). This suggests that Dy(III) ions are also found in the N_3O_6 environment. To get a rough estimation of the distribution we have performed a Curie–Weiss analysis ($\chi_M = C/(T-\theta)$) between 100 and 300 K (Fig. S55†). The best fit is obtained with *C* = 20.99 cm^3 K mol^{-1} (Fig. S55†), from which we estimate the chemical formula $[Dy_{1.41}Nd_{0.59}(hfac)_6(L)]$ with a nona-coordinated site occupation $Dy_{0.41}/Nd_{0.59}$. This proportion of Dy(III) in nine-coordination is slightly higher than the one determined from Scanning Electron Microscopy analysis. Same considerations apply to **16**. With *C* = 17.72 cm^3 K mol^{-1} (Fig. S56†), one finds the chemical formula $[Dy_{1.15}Nd_{0.85}(hfac)_3(tta)_3(L)]$ with nona-coordinated site occupation $Dy_{0.15}/Nd_{0.85}$ in excellent agreement with the Scanning Electron Microscopy analysis. For compound **17**, with Yb(III) ($^2F_{7/2}$: 2.57 cm^3 K mol^{-1}) the chemical formula writes $[Yb_{1.15}Nd_{0.85}(hfac)_6(L)]$ with *C* = 4.35 cm^3 K mol^{-1} (Fig. S57†) also in very good agreement with the Scanning Electron Microscopy analysis. Finally, for **19**, one can write $[Yb_{0.79}Pr_{1.21}(hfac)_6(L)]$ with *C* = 4.52 cm^3 K mol^{-1} and the $^3H_4$ multiplet ground state of Pr(III) (Fig. S58†).

Dynamic measurements. All the compounds have been investigated by ac susceptometry in both zero and applied external dc field. Amongst them, only those which contain Dy(III) ions shows a slowing down of the relaxation of the magnetic moment at low temperature *i.e.* a non-zero the out-of-phase component of the ac susceptibility (χ''_M). Furthermore, for compounds with Dy(III) in N_3O_6 environment (**1**, **2**, **4**, **7**, **9** and **11**), except for **1** (Fig. S59†), no slowing down of the magnetization is observed down to the lowest temperature (2 K) in zero external field. There is, *a priori*, no reason to suspect extra ordinary behavior for Dy(III) in **1** with respect to the other members of the team. The absence of slowing down of the relaxation in zero external field in N_3O_6 environment matches with previous results.[71] In ref. 4, the N_3O_6 environment is strictly identical and is found to relax the most slowly at 1.5 kOe and at 2 K. Thus, the frequency dependences of the magnetic susceptibility at 1.5 kOe are performed in order to compared with our previous study.[70] The results are depicted in Fig. S60–S65† for compounds **1**, **2**, **4**, **7**, **9** and **11**, respectively.

One could qualitatively analyse the frequency maxima values of the four compounds **2**, **4**, **7** and **9** concluding that the slowest magnetic relaxation (40 Hz) is observed for the Dy(III) associated with the transition metal of highest spin state (Mn(II) *S* = 5/2) while more the value of the M(II) spin state is weak more the corresponding system relax faster (Fig. 9 and S60–S65†). Such observation might signify that the dipolar

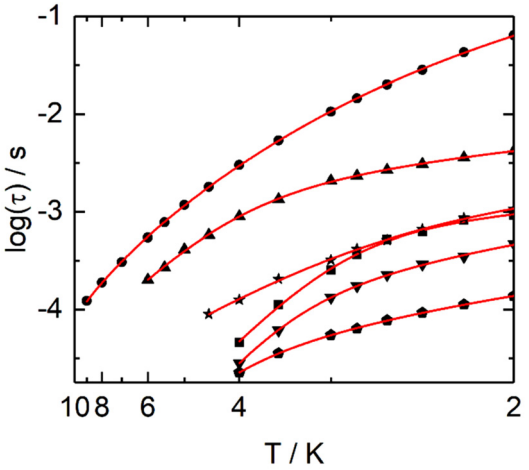

Fig. 9 Arrhenius plots of the relaxation times in a 1500 Oe applied magnetic field for compounds **1** (full circles), **2** (down triangles), **4** (up triangles), **7** (squares), **9** (pentagons) and **11** (stars). Full red lines are the best-fit curves (see text).

interactions between the Dy(III) and associated M(II) ions could play a role on the dynamics of the 3d4f complexes even if effect of weak modification of the crystal field around the lanthanide cannot be rule out. The relaxation time τ was extracted at each temperature using an extended Debye model (details in ESI, Table S11–S15†) in fitting simultaneously the frequency dependence of χ''_M and χ'_M for **1**, **2**, **4**, **7** and **11** or manually selecting the frequencies maxima of χ''_M for **9**. Normalized Cole–Cole plots of the series **1**, **2**, **4**, **7** and **11** are given in Fig. S66–S70.† In-field Arrhenius plots were fitted considering the two thermally dependent Orbach and Raman processes (eqn (1)).

$$\tau^{-1} = \underbrace{CT^n}_{\text{Raman}} + \underbrace{\tau_0{}^{-1} \exp\left(-\frac{\Delta}{KT}\right)}_{\text{Orbach}} \quad (1)$$

The best fits for each of the compounds were obtained with the parameters given in Table S17.† For compounds **1**, **2**, **4**, **7**, **9** and **11**, separated contributions from Orbach and Raman processes are provided in Fig. S70–S76.†

Compound **15** behaves also in a standard way. Indeed, in zero external field it shows slowing down of the relaxation of the magnetic moment which can be safely due to the Dy(III) ions in the N_2O_6 coordination polyhedron made of three $hfac^-$ anions (Fig. S77†).[71] On contrary, the small fraction of Dy(III) ions in the N_3O_6 environment does not contribute in zero field. Once an external field is applied, both octa- and nona-coordinated sites move to lower frequencies with two clear massifs (Fig. S77†) with altitudes that qualitatively fit the 0.41/1 ratio between two sites and the fastest relaxation for the nona-coordinated site.

Furthermore, the high frequency massif appears at the slowest frequency for an external dc field which is close to 1.5 kOe at 2 K as expected from previous studies.[70] The thermal dependence of the relaxation time for each of the Dy centers were extracted from a combination of two extended debye model and the resulting plots fitted with a Raman process while the orbach one became negligible (Fig. S78, Fig. 10, Tables S16 and S17†). Such relaxation of the magnetization for a Dy(III) in D_{4d} N_2O_6 environment is in agreement with what some of us experimentally and computationally determined.[72] One could remark that the n values obtained from our best fits for compounds (**1**, **2**, **4**, **7**, **9**, **11** and **15**) are much lower than the expected n value for Kramers ions (n = 9) (Table S17†). Such value can decrease down to 4, depending on the energies of the ground state doublets.[73,74] Recently, such exponent reduced close to 2 because of the presence of both acoustic and optic phonons in specific ligand environments.[75]

In compound **16**, the nona-coordinated site is only occupied by 15% of Dy(III) which is a too low value to clearly be identified from ac magnetometry and therefore only the octa-coordinated site might be observed. According to ref. 4, Dy(III) in N_2O_6 environment made of two tta^- and one $hfac^-$ ligands should relax at 1 Hz at 2 K and 3 kOe with an amplitude at the maximum of χ''_M slightly below 0.8 cm^3 mol^{-1}. This is close to what we observe for **16** (Fig. S79†) with the maximum falling at

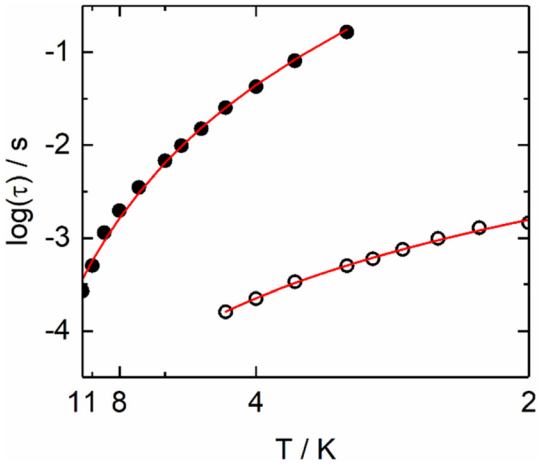

Fig. 10 Arrhenius plots of the relaxation times in a 1500 Oe applied magnetic field for Dy1 (full circles) and Dy2 (open circles) metallic sites in **15**.

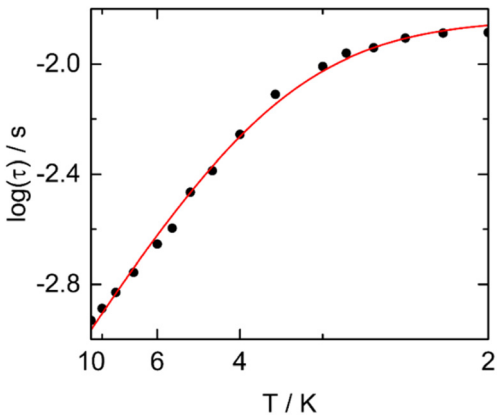

Fig. 11 Arrhenius plots of the relaxation times in a 3000 Oe applied magnetic field for the Dy1 metallic site in **16**.

10 Hz in the same sample environment and a magnetic relaxation for Dy1 (Fig. 11) which occurs through an Orbach (Table S17†) and remaining QTM (τ_{TI} = 0.0146(6) s) processes as previously observed for Dy(III) in N_2O_6 environment made of two tta^- and one $hfac^-$ ligands.[70]

Conclusions

In the previous lines, it was demonstrated that the ligand 2-(1-(2,6-di(pyrazol-1-yl)-4-methylpyridyl)-4,5-(4,5-bis(propylthio)-tetrathiafulvalenyl)-1*H*-benzimidazol-2-yl)-pyridine is suitable for the design of d4f and 4f4f′ heteroleptic complexes through selective coordination on both benzoimidazolylpyridine (bzip) and 2,6-di(pyrazol-1-yl)-4-pyridine (dpp) moieties. The key parameter of the coordination selection for the d–4f complexes is the difference of coordination number between transition metals (coordination number = 6) and lanthanide ions (coordination number = 8, 9) while for the 4f–4f′ complexes the key

parameter is the radius size. All the heterobimetallic complexes involving eight or nine-coordinated Dy(III) ion displayed field-induced SMM with a slight influence of the spin state value of the associated transition metal through dipolar interactions and/or weak change of electronic distribution around the 4f ion. In a photo-physical point of view, the use of the Yb(III) in the design of the 3d–4f complexes leads to an intense, moderated or quenched $^2F_{5/2} \rightarrow {}^2F_{7/2}$ NIR luminescence depending if the Yb(III) ion is respectively associated with the Zn(II), Mn(II) or Ni(II)/Co(II) ion. Light irradiation at 600 nm provokes the observation of the $^4F_{3/2} \rightarrow {}^4I_{13/2}/{}^4I_{11/2}/{}^4I_{9/2}$ Nd(III) centred emission for the $[Dy_{1.21}Nd_{0.79}(hfac)_6(L)]\cdot 2(CH_2Cl_2)\cdot(C_6H_{14})$ complex and the $^2F_{5/2} \rightarrow {}^2F_{7/2}$ Yb(III) centred emission for the [YbPr(hfac)$_6$(L)] complex. When the Pr(III) ion is replaced by the Nd(III) ion ([$Yb_{1.04}Nd_{0.96}$(hfac)$_6$(L)]) no dual NIR emission is detected.

Finally the compound **15** displayed both slow magnetic relaxation and NIR luminescence and can be described as a field-induced luminescent single-molecule magnet.

Author contributions

H. D. and B. L. performed the organic syntheses, the coordination chemistry and crystallisations; V. D. realised the single crystal X-ray diffraction experiments and refined the X-ray structures; J. F. G. and O. C. performed and analysed the magnetic measurements; S. S., F. R., O. M. performed and analysed the photophysical measurements; A. G., B. L. G. and V. M. discussed the idea and the results and commented on the manuscript; F. P. and O. C. contributed to the writing of the article. F. P. conceived and designed the experiments and was granted of the ANR and ERC funded projects.

Conflicts of interest

There are no conflicts to declare.

Acknowledgements

This work was supported by Région Bretagne, Rennes Métropole, CNRS, Université de Rennes 1, FEDER, the ANR (ANR-13-BS07-0022-01) and the European Commission through the ERC-CoG 725184 MULTIPROSMM (project no. 725184). S. S. would like to thank Obra Social de la Fundació "La Caixa" and Fundació Universitària Agustí Pedro i Pons for financial support.

References

1 C. Piguet and J.-C. G. Bünzli, *Chem. Soc. Rev.*, 1999, **28**, 347–358.
2 S. Comby and J.-C. G. Bünzli, *Handbook on the Physics and Chemistry of Rare Earths*, Elsevier BV, Amsterdam, The Netherland, 2007, ch. 235, vol. 37.
3 D. Gatteschi, R. Sessoli and J. Villain, *Molecular Nanomagnets*, Oxford University Press, New York, 2006.
4 L. Bogani and W. Wernsdorfer, *Nat. Mater.*, 2008, **7**, 179–186.
5 M. Mannini, F. Pineider, P. Sainctavit, C. Danieli, E. Otero, C. Sciancalepore, A. M. Talarico, M.-A. Arrio, A. Cornia, D. Gatteschi and R. Sessoli, *Nat. Mater.*, 2009, **8**, 194–197.
6 M. N. Leuenberger and D. Loss, *Nature*, 2001, **410**, 789–793.
7 J. Lehmann, A. Gaita-Arino, E. Coronado and D. Loss, *Nat. Nanotechnol.*, 2007, **2**, 312–317.
8 M. Ganzhorn, S. Klyatskaya, M. Ruben and W. Wernsdorfer, *Nat. Nanotechnol.*, 2013, **8**, 165–169.
9 K. Kuriki, Y. Koike and Y. Okamoto, *Chem. Rev.*, 2002, **102**, 2347–2356.
10 E. G. Moore, A. P. S. Samuel and K. N. Raymond, *Acc. Chem. Res.*, 2009, **42**, 542–552 and references therein.
11 J.-C. G. Bünzli, *Chem. Rev.*, 2010, **110**, 2729–2755.
12 R. M. Duke, E. B. Veale, F. M. Pfeffer, P. E. Kruger and T. Gunnlaugsson, *Chem. Soc. Rev.*, 2010, **39**, 3936–3953.
13 A. Beeby, S. W. Botchway, I. M. Clarkson, S. Faulkner, A. M. Parker, D. Parker and J. A. G. Williams, *J. Photochem. Photobiol., B*, 2000, **57**, 83–89.
14 A. Grichine, A. Haefele, S. Pascal, A. Duperray, R. Michel, C. Andraud and O. Maury, *Chem. Sci.*, 2014, **5**, 3475–3485.
15 R. Sessoli and A. K. Powell, *Coord. Chem. Rev.*, 2009, **253**, 2328–2341.
16 T. N. Hooper, J. Schnack, S. Piligkos, M. Evangelesti and E. K. Brechin, *Angew. Chem., Int. Ed.*, 2012, **51**, 4633–4636.
17 J. W. Sharples and D. Collison, *Coord. Chem. Rev.*, 2014, **260**, 1–20.
18 K. R. Vignesh, S. K. Langley, K. S. Murray and G. Rajaraman, *Chem. – Eur. J.*, 2017, **23**, 1654–1166.
19 H. L. C. Feltham and S. Brooker, *Coord. Chem. Rev.*, 2014, **276**, 1–33.
20 I. Oyarzabal, J. Ruiz, E. Ruiz, D. Aravena, J. Seco and E. Colacio, *Chem. Commun.*, 2015, **51**, 12353–12356.
21 W.-B. Sun, P.-F. Yan, S.-D. Jiang, B.-W. Wang, Y.-Q. Zhang, H.-F. Li, P. Chen, Z.-M. Wang and S. Gao, *Chem. Sci.*, 2016, **7**, 684–691.
22 M. Shamugam, A. Upadhyay, C. Das, S. Vaidya, S. K. Singh, T. Gupta, R. Mondal, S. Langley, K. Murray and G. Rajaraman, *Chem. – Eur. J.*, 2017, **23**, 4903–4916.
23 J.-D. Leng, J.-L. Liu, Y.-Z. Zheng, L. Ungur, L. F. Chibotaru, F.-S. Guo and M.-L. Tong, *Chem. Commun.*, 2013, **49**, 158–160.
24 Q.-W. Li, J.-L. Liu, J.-H. Jia, J.-D. Leng, W.-Q. Lin, Y.-C. Chen and M.-L. Tong, *Dalton Trans.*, 2013, **42**, 11262.
25 F. Pointillart, O. Cador, B. Le Guennic and L. Ouahab, *Coord. Chem. Rev.*, 2017, **346**, 150–175.
26 C. Edder, C. Piguet, G. Bernardinelli, J. Mareda, C. Bochet, J.-C. G. Bünzli and G. Hopfgartner, *Inorg. Chem.*, 2000, **39**, 5059–5073.
27 J. H. van Vleck, *J. Phys. Chem.*, 1937, **41**, 67–80.
28 A. D'Aléo, F. Pointillart, L. Ouahab, C. Andraud and O. Maury, *Coord. Chem. Rev.*, 2012, **256**, 1604–1620.

29 F. Pointillart, B. Le Guennic, O. Cador, O. Maury and L. Ouahab, *Acc. Chem. Res.*, 2015, **48**, 2834–2842.
30 S. Faulkner and S. J. Pope, *J. Am. Chem. Soc.*, 2003, **125**, 10526–10527.
31 T. J. Sørensen, M. Tropiano, O. A. Blackburn, J. A. Tilney, A. M. Kenwright and S. Faulkner, *Chem. Commun.*, 2013, **49**, 783–785.
32 J. Long, R. Vallat, R. A. S. Ferreira, L. D. Carlos, F. A. Almeida Paz, Y. Guari and J. Larionova, *Chem. Commun.*, 2012, **48**, 9974–9976.
33 D. Imbert, M. Cantuel, J.-C. G. Bünzli, G. Bernardinelli and C. Piguet, *J. Am. Chem. Soc.*, 2003, **125**, 15698–15699.
34 D. Zare, Y. Suffren, H. Nozary, A. Hauser and C. Piguet, *Angew. Chem., Int. Ed.*, 2017, **56**, 14612–14617.
35 H.-R. Wen, P.-P. Dong, S.-J. Liu, J.-S. Liao, F.-Y. Liang and C.-M. Liu, *Dalton Trans.*, 2017, **46**, 1153–1162.
36 Y. Liu, Y.-C. Chen, J. Liu, W.-B. Chen, G.-Z. Huang, S.-G. Wu, J. Wang, J.-L. Liu and M.-L. Tong, *Inorg. Chem.*, 2020, **59**, 687–694.
37 K. Fan, S.-S. Bao, R. Huo, X.-D. Huang, Y.-J. Liu, Z.-W. Yu, M. Kurmoo and L.-M. Zheng, *Inorg. Chem. Front.*, 2020, **7**, 4580–4592.
38 J. Wang, J. J. Zakrzewski, M. Zychowicz, V. Vieru, L. F. Chibotaru, K. Nakabayashi, S. Chorazy and S. Ohkoshi, *Chem. Sci.*, 2021, **12**, 730–741.
39 N. André, T. B. Jensen, R. Scopelliti, D. Imbert, M. Elhabiri, G. Hopfgartner, C. Piguet and J.-C. G. Bünzli, *Inorg. Chem.*, 2004, **43**, 515–529.
40 N. Dalla-Favera, J. Hamacek, M. Borkovec, D. Jeannerat, G. Ercolani and C. Piguet, *Inorg. Chem.*, 2007, **46**, 9312–9322.
41 P. E. Ryan, G. Canard, S. Koeller, B. Bocquet and C. Piguet, *Inorg. Chem.*, 2012, **51**, 10012–10024.
42 R. E. P. Winpenny, *Chem. Soc. Rev.*, 1998, **27**, 447–452.
43 M. Sakamoto, K. Manseki and H. Okawa, *Coord. Chem. Rev.*, 2001, **219**, 379–414.
44 C. Benelli and D. Gatteschi, *Chem. Rev.*, 2002, **102**, 2369–2388.
45 M. Andruh, J. P. Costes, C. Diaz and S. Gao, *Inorg. Chem.*, 2009, **48**, 3342–3359 (Forum Article).
46 M. Andruh, *Chem. Commun.*, 2011, **47**, 3025–3042.
47 L. Sorace, C. Benelli and D. Gatteschi, *Chem. Soc. Rev.*, 2011, **40**, 3092–3104.
48 T. J. Sorensen and S. Faulkner, *Acc. Chem. Res.*, 2018, **51**, 2493–2501.
49 G. Cosquer, F. Pointillart, Y. Le Gal, S. Golhen, O. Cador and L. Ouahab, *Chem. – Eur. J.*, 2011, **17**, 12502–12511.
50 G. Cosquer, F. Pointillart, B. Le Guennic, Y. Le Gal, S. Golhen, O. Cador and L. Ouahab, *Inorg. Chem.*, 2012, **51**, 8488–8501.
51 M. Feng, F. Pointillart, B. Lefeuvre, V. Dorcet, S. Golhen, O. Cador and L. Ouahab, *Inorg. Chem.*, 2015, **54**, 4021–4028.
52 S. Speed, M. Feng, G. Fernandez-Garcia, F. Pointillart, B. Lefeuvre, F. Riobé, S. Golhen, B. Le Guennic, F. Totti, Y. Guyot, O. Cador, O. Maury and L. Ouahab, *Inorg. Chem. Front.*, 2017, **4**, 604–617.
53 M. Llunell, D. Casanova, J. Cirera, J. M. Bofill, P. Alemany and S. Alvarez, *S. SHAPE (version 2.1)*, Barcelona, 2013.
54 G. Cosquer, F. Pointillart, J. Jung, B. Le Guennic, S. Golhen, O. Cador, Y. Guyot, A. Brenier, O. Maury and L. Ouahab, *Eur. J. Inorg. Chem.*, 2014, 69–82.
55 P. Goldner, F. Pell, D. Meichenin and F. Auzel, *J. Lumin.*, 1997, **71**, 137–150.
56 X. Yi, K. Bernot, V. Le Corre, G. Calvez, F. Pointillart, O. Cador, B. Le Guennic, J. Jung, O. Maury, V. Placide, Y. Guyot, T. Roisnel, C. Daiguebonne and O. Guillou, *Chem. – Eur. J.*, 2014, **20**, 1569–1576.
57 L. Tian, M. Zhang, P. Lu, W. Zhang, B. Yang and Y. Ma, *Chin. Sci. Bull.*, 2004, **49**, 246–248.
58 T. D. Pasatoiu, C. Tiseanu, A. M. Madalan, B. Jurca, C. Duhayon, J.-P. Sutter and M. Andruh, *Inorg. Chem.*, 2011, **50**, 5879–5889.
59 O. Maury, J.-P. Guégan, T. Renouard, A. Hilton, P. Dupau, N. Sandon, L. Toupet and H. Le Bozec, *New J. Chem.*, 2001, **25**, 1553–1566.
60 J. Song, C.-R. Li, Q. Xu, X.-T. Xu, L.-X. Sun and Y.-H. Xing, *Spectrochim. Acta, Part A*, 2015, **150**, 308–315.
61 M. Maity, M. C. Majee, S. Kundu, S. K. Samanta, E. C. Sanudo, S. Ghosh and M. Chaudhury, *Inorg. Chem.*, 2015, **54**, 9715–9726.
62 T. Förster, *Faraday Soc.*, 1959, **27**, 7–17.
63 F. Artizzu, A. Serpe, L. Marchio, M. Saba, A. Mura, M. L. Mercuri, G. Bongiovanni, P. Deplano and F. Quochi, *J. Mater. Chem. C*, 2015, **3**, 11524–11530.
64 A. D. Sontakke, K. Biswas, R. Sen and K. Annapurna, *Opt. Mater.*, 2010, **32**, 1333–1336.
65 R.-X. Chen, T. Gao, W.-B. Sun, H.-F. Li, Y.-H. Wu, M.-M. Xu, X.-Y. Zou and P.-F. Yan, *Inorg. Chem. Commun.*, 2015, **56**, 79–82.
66 L. Abad Galan, D. Aguila, Y. Guyot, V. Velasco, O. Roubeau, S. T. Teat, M. Massi and G. Aromi, *Chem. – Eur. J.*, 2021, **27**, 7288–7299.
67 O. Kahn, *Molecular Magnetism*, VCH, 1993.
68 R. Orbach, *Proc. R. Soc. London, Ser. A*, 1961, **264**, 458–484.
69 A. Abragam and B. Bleaney, *Electron Paramagnetic Resonance of Transition Ions*, Oxford University Press, Oxford, Reprint edn, 2012.
70 M. Feng, F. Pointillart, B. Lefeuvre, V. Dorcet, S. Golhen, O. Cador and L. Ouahab, *Inorg. Chem.*, 2015, **54**, 4021–4028.
71 G. Cosquer, F. Pointillart, S. Golhen, O. Cador and L. Ouahab, *Chem. – Eur. J.*, 2013, **19**, 7895–7903.
72 F. Pointillart, J.-K. Ou-Yang, G. Fernandez-Garcia, V. Montigaud, J. Flores Gonzalez, R. Marchal, L. Favereau, F. Totti, J. Crassous, O. Cador, L. Ouahab and B. Le Guennic, *Inorg. Chem.*, 2019, **58**, 52–56.
73 C. Dekker, A. F. M. Arts, H. W. de Wijn, A. J. van Duyneveldt and J. A. Mydosh, *Phys. Rev. B: Condens. Matter Mater. Phys.*, 1989, **40**, 11243–11251.
74 J. Tang and P. Zhang, *Lanthanide single molecule magnets*, Springer, 2015.
75 C. A. P. Goodwin, D. Reta, F. Ortu, N. F. Chilton and D. P. Mills, *J. Am. Chem. Soc.*, 2017, **139**, 18714–18724.

